

Correlation Effects in a Simplified Bilayer Two-Orbital Hubbard Model at Half Filling

Jian-Jian Yang, Dao-Xin Yao,^{*} and Han-Qing Wu[†]

Guangdong Provincial Key Laboratory of Magnetoelectric Physics and Devices,
State Key Laboratory of Optoelectronic Materials and Technologies, Center for Neutron Science and Technology,
School of Physics, Sun Yat-sen University, Guangzhou 510275, China

(Dated: August 23, 2024)

Motivated by recent findings indicating high-temperature superconductivity in bilayer nickelate $\text{La}_3\text{Ni}_2\text{O}_7$ under pressures, we employ projective formalism of determinant quantum Monte Carlo simulations to explore the ground-state phase diagram and correlation effects using a simplified bilayer two-orbital Hubbard model at half filling. Our numerical results reveal the instability of the metallic phase under weak on-site Hubbard U , leading to the emergence of a nonmagnetic weakly insulating phase without breaking any symmetry. As the U increases, an antiferromagnetic Mott insulating phase emerges when the ratio U/t_1^x exceeds approximately 4.15. This magnetic phase transition belongs to the 3D $O(3)$ Heisenberg universality class. Furthermore, using analytical continuation, we explore the dynamical properties, such as the single-particle spectral function and dynamical spin structure factor, pertinent to experimental investigations. Our numerical results can help to understand the strong correlation effects within $\text{La}_3\text{Ni}_2\text{O}_7$.

Introduction.—Recently, a new type of nickelate, $\text{La}_3\text{Ni}_2\text{O}_7$, has been discovered to exhibit superconductivity exceeding the boiling temperature of liquid nitrogen under high pressures [1]. Subsequent theoretical study further characterized the electronic structure of $\text{La}_3\text{Ni}_2\text{O}_7$ using a bilayer two-orbital model [2]. Up to now, there are several experimental works [3–8] have confirmed the zero resistance below T_c , and in addition, some theoretical studies [9–24] have revealed the pairing symmetry. For the latest advancements on this material, one can refer to some review articles [25, 26]. The basic structure of $\text{La}_3\text{Ni}_2\text{O}_7$ crystal is Ni-O bilayer, in which six oxygen ions around each Ni ion form an octahedron [1]. The Ni- e_g and $-t_{2g}$ orbitals are well separated by octahedral crystal field, resulting in the energy of e_g orbitals being higher than that of t_{2g} . Taking into account the electronic configuration of Ni- $d^{7.5}$ (a mixture of d^7 and d^8), the t_{2g} orbitals are full-filled, while e_g should be partially filled. The electronic structure of $\text{La}_3\text{Ni}_2\text{O}_7$ can be effectively described by a bilayer two-orbital model containing Ni- $d_{x^2-y^2}$ and $-d_{3z^2-r^2}$ orbitals [2, 10]. The bilayer two-orbital model has been widely used in theoretical research for $\text{La}_3\text{Ni}_2\text{O}_7$ [9–20, 27–33].

In addition to being an important model for $\text{La}_3\text{Ni}_2\text{O}_7$, from a theoretical perspective, the bilayer two-orbital model also offers a unique Fermi surface that serves as a platform for investigating the ground state phase diagram and interaction induced correlation effects. However, the determinant quantum Monte Carlo (DQMC) simulation on original bilayer two-orbital model encounters a sign problem, which prevents DQMC to study its ground-state properties in large system sizes. To avoid this, we employ a simplified, half-filled bilayer two-orbital Hubbard model to study correlation effects. Although this simplified model may not fully capture the superconductivity in $\text{La}_3\text{Ni}_2\text{O}_7$, it is expected to reveal similar properties that could aid in understanding the electronic

correlations within this material. Experimentally, tuning the electron doping may drive both the $d_{x^2-y^2}$ orbital and the $d_{3z^2-r^2}$ orbital in $\text{La}_3\text{Ni}_2\text{O}_7$ material into half-filling case [14].

In this paper, we employ a projective formalism of determinant quantum Monte Carlo method to do the large-scale simulations on the ground-state phase diagram and dynamical properties of a simplified bilayer two-orbital model at half-filling. The ground-state phase diagram is composed of an antiferromagnetic Mott insulator (AFMI) at $U > U_c$, a metallic phase in the non-interaction limit $U = 0$ and a nonmagnetic weakly insulating (WI) phase in the intermediate $0 < U < U_c$ region. Careful finite-size scaling analysis indicates the magnetic transition between WI and AFMI belongs to (2+1)D classical Heisenberg universality class. We also study the single-particle spectrum and dynamic spin structure factor and make some connection to the experimental results of $\text{La}_3\text{Ni}_2\text{O}_7$, like angle resolved photoemission spectroscopy (ARPES) and inelastic neutron scattering (INS).

Model and method.—The Hamiltonian of bilayer two-orbital Hubbard model [Fig. 1(a)] can be written as

$$H = \sum_{\langle i,j \rangle, \sigma} \sum_{m\alpha, n\lambda} t_{ij}^{m\alpha, n\lambda} c_{im\alpha\sigma}^\dagger c_{jn\lambda\sigma} + U \sum_{i, m\alpha} (n_{im\alpha\uparrow} - \frac{1}{2})(n_{im\alpha\downarrow} - \frac{1}{2}),$$

where $c_{im\alpha\sigma}^\dagger$ ($c_{im\alpha\sigma}$) creates (annihilates) an electron with spin- σ at the α orbital of layer m in the i -th unit cell, and $n_{im\alpha\sigma} = c_{im\alpha\sigma}^\dagger c_{im\alpha\sigma}$ is particle number operator. $U > 0$ is on-site Coulomb repulsive interaction which is set to the same value for each orbitals. $t_{ij}^{m\alpha, n\lambda}$ represent hopping integrals [see Fig. 1(a)], the values of which are set to be $t_1^x = 1$ (as energy unit), $t_1^z = 0.228$, $t_3^{xz} = 0.495$ and $t_1^z = 1.315$, ratios of which are inherited

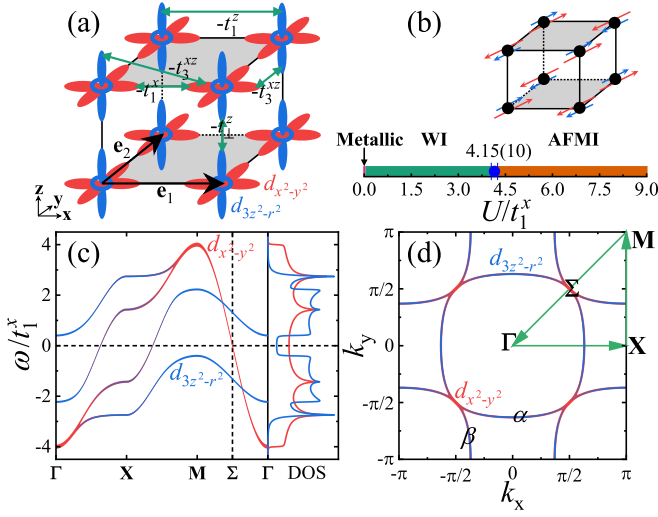


FIG. 1. (a) Illustration of simplified bilayer two-orbital model which contains $d_{x^2-y^2}$ (red) and $d_{3z^2-r^2}$ (blue) orbitals. Here $\mathbf{e}_1 = (1, 0)a$, $\mathbf{e}_2 = (0, 1)a$ are primitive vectors, and $a \equiv 1$ is the lattice constant which is the length unit. (b) Ground-state phase diagram. There are three phases: $U = 0$ metallic phase, weakly insulating (WI) phase and antiferromagnetic Mott insulator (AFMI) phase. In the upper right corner is the configuration of AFMI order, where the red and blue arrows indicate the magnitude and direction of the magnetic moments for $d_{x^2-y^2}$ and $d_{3z^2-r^2}$ orbitals, respectively. (c) Band structure and local density of states in the noninteracting limit. The red and blue color represent the contributions from $d_{x^2-y^2}$ and $d_{3z^2-r^2}$ orbitals, respectively. (d) Fermi surface at $U = 0$ in the first Brillouin zone. Only the $d_{x^2-y^2}$ orbital contributes to the density of state in Σ point at the Fermi level.

from Ref. [2]. But the $d_{x^2-y^2}$ and $d_{3z^2-r^2}$ orbitals are both at half filling in our case.

In the noninteracting case, the system is in a metallic phase with finite density of states at the Fermi level, as shown in Fig. 1(c). The Fermi surface consists a α pocket centering around Γ point and a β pocket centering around \mathbf{M} point, and these two convex Fermi surfaces are perfectly nesting with nesting wave vector $\mathbf{q} = (\pi, \pi)$. Moreover, these two Fermi surface touch at Σ point. At this special point, there is only the contribution from $d_{x^2-y^2}$ orbital. And this Fermi surface is topologically equivalent to the $\text{La}_3\text{Ni}_2\text{O}_7$ under ambient pressure [34, 35].

When $U > 0$, the projective formalism of determinant quantum Monte Carlo (DQMC) algorithm is employed to study the ground-state phases and their excitation, with details provided in Refs. [36–38]. At half filling, due to particle-hole symmetry and time-reversal symmetry, there is no sign problem in DQMC simulations. To reduce the finite-size effect, two types of clusters are used in this study. The first type is expanded by primitive vectors \mathbf{e}_1 and \mathbf{e}_2 , its linear cluster size is denoted by L , and the number of unit cells $N_c = L^2$. The cluster size for this kind of lattice is up to $L = 14$. And the second type

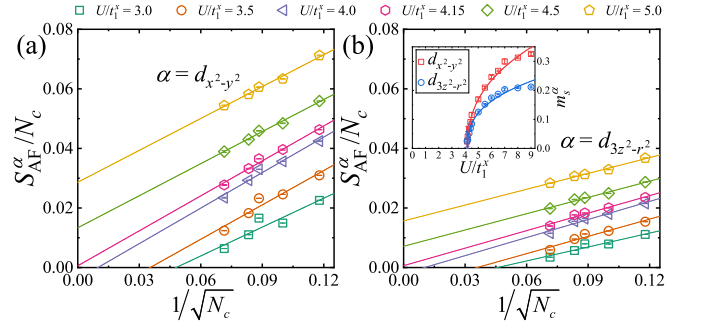


FIG. 2. Linear extrapolations of spin structure factors S_{AF}^α/N_c for (a) $d_{x^2-y^2}$ and (b) $d_{3z^2-r^2}$ orbitals. The linear cluster sizes used here are $L = 10, 12, 14$ and $L' = 6, 8$. Inset: Finite staggered magnetization as functions of U .

of clusters is expanded by $\mathbf{a}_1 = (-1, 1)a$ and $\mathbf{a}_2 = (1, 1)a$ lattice vectors, its linear cluster size is denoted by L' , and the number of unit cells is $N_c = 2L'^2$, and the cluster size for this kind of lattice is up to $L' = 8$. The principle we choose the lattices is that these lattices can take the \mathbf{M} or Σ wave vectors. These two wave vectors are important for detecting the magnetic order and the insulating behavior under Hubbard U interaction. In addition, unless otherwise stated, the simulations are done using periodic boundary condition (PBC).

Magnetic transition.—The spin structure factor, written as $S^\alpha(\mathbf{k}) = (1/2N_c) \sum_{i,j,m} e^{-i\mathbf{k}\cdot(\mathbf{R}_j-\mathbf{R}_i)} \langle \mathbf{S}_{i\mathbf{m}\alpha} \cdot \mathbf{S}_{j\mathbf{m}\alpha} \rangle$, can be used to detect the magnetic ordering, where $\mathbf{S}_{i\mathbf{m}\alpha} = (1/2) \sum_{\sigma,\sigma'} c_{i\mathbf{m}\alpha\sigma}^\dagger [\boldsymbol{\sigma}]_{\sigma\sigma'} c_{i\mathbf{m}\alpha\sigma'}$ is spin operator with Pauli matrix $\boldsymbol{\sigma} = (\sigma_x, \sigma_y, \sigma_z)$. In the strong interaction region, an antiferromagnetic (AF) order is expected in the system, corresponding to a divergent tendency in spin structure factor at point \mathbf{M} , i.e., $S_{\text{AF}}^\alpha = S^\alpha(\mathbf{M})$. And the staggered magnetization (between the same orbital) can be estimated as $m_s^\alpha = \lim_{N_c \rightarrow \infty} \sqrt{S_{\text{AF}}^\alpha/N_c}$. The linear extrapolations of S_{AF}^α/N_c are shown in Fig. 2. As the interaction strength increases to $U/t_1^x \approx 4.15$, both $d_{x^2-y^2}$ and $d_{3z^2-r^2}$ orbitals evolve from nonmagnetic states to AF long-range orders, suggesting nearly the same magnetic transition point $U_c/t_1^x = 4.15(10)$ for both orbitals. The staggered magnetization as functions of U for different orbitals are shown in the inset of Fig. 2(b), where the solid lines represent the fitting functions using $m_s^\alpha \propto (U - U_c)^\beta$ [39]. We will discuss the critical behavior of this phase transition in the later section. The configuration of AFM order is shown in the upper panel of Fig. 1(b), the magnetic orders of two orbitals within the same unit cell and the same layer ferromagnetically align to each other and the extrapolated staggered magnetization of two orbitals are estimated to retain 38% and 24% of their classical orders at $U/t_1^x = 9.0$.

Weakly interacting region.—After identifying the magnetic transition at finite U , important questions arise: whether the metallic phase in the non-interacting limit

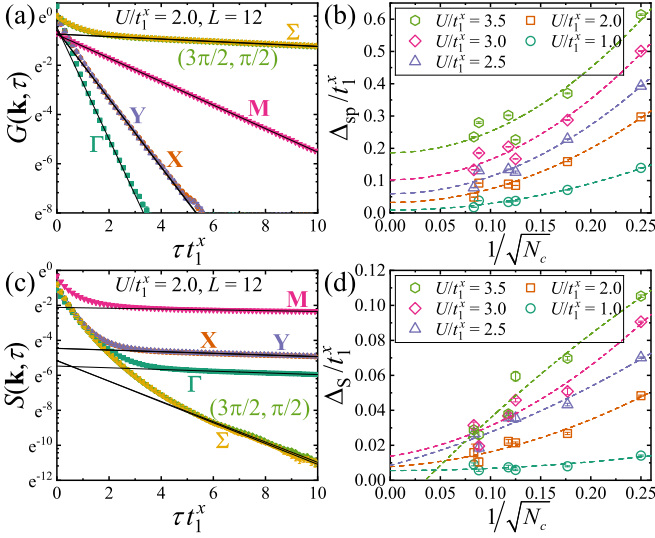


FIG. 3. (a) Imaginary time-displaced single-particle Green's function $G(\mathbf{k}, \tau)$ and (c) imaginary time-displaced spin correlation function $S(\mathbf{k}, \tau)$ at high-symmetry points are shown with semilog type for $U/t_1^x = 2.0$ and $L = 12$, where $Y = (0, \pi)$, and the black solid lines represent linear fitting of the tails to get the corresponding gaps. Second-order polynomial extrapolations of (b) single-particle gap Δ_{sp} and (d) spin gap Δ_S with some constraints.

can survive in the weakly interacting ($0 < U < U_c$) region, and whether the magnetic transition occurs between two insulating phases or synchronizes with the metal-insulator transition. A straightforward way to answer these questions is by calculating the single-particle gap Δ_{sp} , which can be extracted from the imaginary time displaced single-particle Green's function $G(\mathbf{k}, \tau) = (1/4N_c) \sum_{i,j,m\alpha,\sigma} e^{-i\mathbf{k}\cdot(\mathbf{R}_j - \mathbf{R}_i)} \langle c_{im\alpha\sigma}^\dagger(\tau) c_{jm\alpha\sigma}(0) \rangle$, and $c_{im\alpha\sigma}^\dagger(\tau) = e^{\tau H} c_{im\alpha\sigma}^\dagger e^{-\tau H}$, where τ is the imaginary time. When τ is sufficiently large, there is $G(\mathbf{k}, \tau) \propto e^{-\tau \Delta_{\text{sp}}(\mathbf{k})}$. As shown in Fig. 3(a), the smallest gap is taken at Σ point in the finite-size systems. The finite-size extrapolations of Δ_{sp} are shown in Fig. 3(b). Due to the presence of fluctuating size-dependent behavior, we have use a constraint in the least square fitting using second-order polynomial functions. This constraint is that the fitting line should be decreased not upward as $1/\sqrt{N_c}$ goes to zero. The dotted lines are used to show these constraint extrapolation functions. It can be estimated that the single-particle gap is already open at Σ point when $U/t_1^x \geq 1.0$. To clarify whether the single-particle gap is open in the whole Fermi surface simultaneously, we choose $L' = 8$ cluster which contains several Fermi wave vectors (including Σ) in its Brillouin zone. The finite-size single-particle gaps at these Fermi wave vectors are nearly the same in the $0 < U < U_c$ region. This implies that the gap at Σ point can represent the single-particle gap of the system. Therefore, we can make a reasonable conclusion that the system opens a fully single-particle

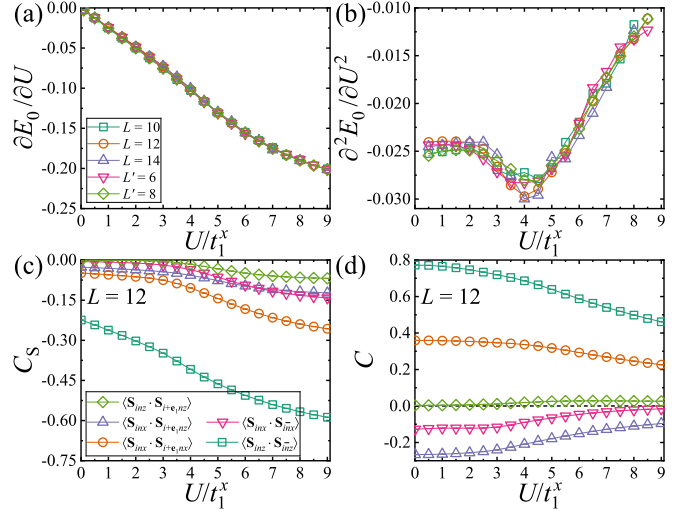


FIG. 4. (a) The first and (b) the second derivatives of energy with respect to U as functions of U for different clusters. (c) Local spin correlations and (d) local single-particle correlations as functions of U for $L = 12$, where the symbols in (d) correspond to the same bond as in (c). Here, the subscripts n and \bar{n} denote the opposite layers, while x and z represent the $d_{x^2-y^2}$ and $d_{3z^2-r^2}$ orbitals, respectively.

gap at the whole Fermi surface and comes into a weakly insulating phase.

Similarly, the spin gap Δ_S can be extracted from the imaginary time-displaced spin correlation function $S(\mathbf{k}, \tau) = (1/4N_c) \sum_{i,j,m\alpha} e^{-i\mathbf{k}\cdot(\mathbf{R}_j - \mathbf{R}_i)} \langle \mathbf{S}_{im\alpha}(\tau) \cdot \mathbf{S}_{jm\alpha}(0) \rangle$, with $S(\mathbf{k}, \tau) \propto e^{-\tau \Delta_S(\mathbf{k})}$ when τ is large enough. As shown in Fig. 3(c), the lowest spin gap is at the \mathbf{M} point, which corresponds to the wave vector of the AF order. Figure 3(d) shows the extrapolations of spin gap Δ_S using second-order polynomial functions with the same constraint. When $U/t_1^x \leq 3.0$, as the U increases, the spin gap increases to a maximum and then decreases to zero in the AF phase due to gapless Goldstone mode related to spontaneously $SU(2)$ symmetry breaking. The extrapolated negative spin gap at $U/t_1^x = 3.5 < U_c/t_1^x$ may due to the finite-size effects. In a word, Fig. 3(b) and Fig. 3(d) support a gapped phase in the weakly interacting region and the existence of a finite U magnetic transition between two insulating phases.

To identify that there is no quantum phase transition at $0 < U < U_c$, we measure a quantity that is not explicitly dependent on wave vectors, the first derivative of energy E_0 , $\partial E_0/\partial U = (1/4N_c) \sum_{i,m\alpha} \langle (n_{im\alpha\uparrow} - 1/2)(n_{im\alpha\downarrow} - 1/2) \rangle$ with $E_0 = \langle H \rangle / (4N_c)$, whose discontinuity can be used to characterize phase transitions [40–44]. The $\partial E_0/\partial U$ as functions of U for different clusters are shown in Fig. 4(a). It can be observed that $\partial E_0/\partial U$ decreases monotonically with U , and its numerical first derivative, i.e., the second derivative of energy [Fig. 4(b)], shows only one peak around the magnetic

transition point U_c . That means there would be no other quantum phase transition between $0 < U < U_c$.

To further characterize the weakly insulating phase in the $0 < U < U_c$ region, we have done the extrapolations of conventional orders, like charge density wave, pair density wave, inter-layer exciton and bond-order wave. They all extrapolate to zero. It is a featureless insulating phase. In this ground state, the $d_{3z^2-r^2}$ orbitals are closely forming the direct product of the ground state of two-site Hubbard model, $[(c_{i1z\uparrow}^\dagger c_{i2z\downarrow}^\dagger - c_{i1z\downarrow}^\dagger c_{i2z\uparrow}^\dagger) + g(c_{i1z\uparrow}^\dagger c_{i1z\downarrow}^\dagger + c_{i2z\uparrow}^\dagger c_{i2z\downarrow}^\dagger)]|0\rangle/\sqrt{2+2g^2}$ with $g = (\sqrt{U^2 + 16t_\perp^2} - U)/(4t_\perp^z)$, due to the strong hopping ratios $|t_\perp^z/t_\perp^x| = 5.768$ and $|t_\perp^z/t_3^{xz}| = 2.657$. But owing to the hybridization t_3^{xz} between two nearby $d_{3z^2-r^2}$ and $d_{x^2-y^2}$ orbitals, the $d_{x^2-y^2}$ orbital can also generate a mass gap to form insulating phase. This weakly insulating phase may belong to a kind of symmetric mass generation (SMG) phase without symmetry breaking [45–49]. In Figs. 4(c) and 4(d), we show the real-space spin correlations $C_S = \langle \mathbf{S}_{im\alpha} \cdot \mathbf{S}_{jn\lambda} \rangle$ and single-particle correlations $C = (1/2) \sum_\sigma \langle c_{im\alpha\sigma}^\dagger c_{jn\lambda\sigma} + H.c. \rangle$ as functions of U , respectively. It is noted that despite the nonzero value of the hopping t_\perp^z between intra-layer $d_{3z^2-r^2}$ orbitals, their spin correlation nearly remains zero from $U/t_1^x = 0$ to a finite U . As a comparison, the inter-layer $d_{3z^2-r^2}$ orbitals have the strongest spin correlation $\langle \mathbf{S}_{inz} \cdot \mathbf{S}_{i\bar{n}z} \rangle$ and single-particle correlation $\sum_\sigma \langle c_{inz\sigma}^\dagger c_{i\bar{n}z\sigma} + H.c. \rangle$. When U gets larger, its correlation strength increases more near to $-3/4$ indicating inter-layer $d_{3z^2-r^2}$ orbitals are more likely to form inter-layer singlets $(c_{i1z\uparrow}^\dagger c_{i2z\downarrow}^\dagger - c_{i1z\downarrow}^\dagger c_{i2z\uparrow}^\dagger)|0\rangle/\sqrt{2}$ and suppress magnetic order.

Critical behavior.—From the perspective of symmetry analysis, the transition from WI phase with charge and spin gaps to AFM phase which breaks the $SU(2)$ spin rotation symmetry belongs to the 3D $O(3)$ universality class. By employing the standard scaling analysis $S_{AF}^\alpha/N_c = L^{-2\beta/\nu} f[L^{1/\nu}(U - U_c)/U_c]$, we investigate the critical behavior of the WI-AFMI transition. Here, β and ν are critical exponents, and $f[L^{1/\nu}(U - U_c)/U_c]$ represents scaling function. The optimal critical parameters

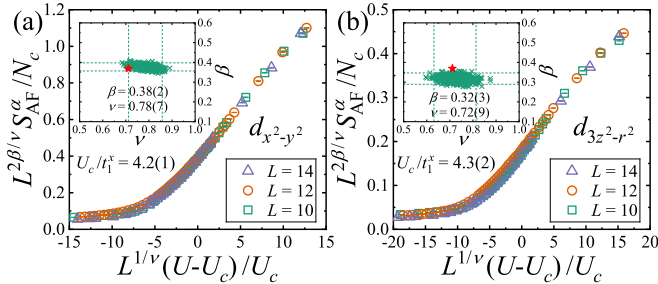


FIG. 5. Finite-size scaling of spin structure factor at (a) $d_{x^2-y^2}$ and (b) $d_{3z^2-r^2}$ orbitals. The critical exponents are near to the 3D $O(3)$ Heisenberg universality class.

are obtained through Bayesian scaling analysis based on Gaussian process regression [50, 51], and the results of data collapse are illustrated in Fig. 5, where the confidence interval estimations are derived from Monte Carlo sampling. The quantum critical point here is close to the one got from extrapolations of spin structure factor $U_c/t_1^x \approx 4.15$, supporting the presence of a finite U magnetic transition. The critical exponents are close to those of the 3D $O(3)$ Heisenberg universality class [52] with slight deviation. The deviations of critical exponents may be due to the limitation of finite-size lattices [53].

Dynamic excitation spectra.—The single-particle spectral function $A(\mathbf{k}, \omega)$ and dynamic spin structure factor $S(\mathbf{k}, \omega)$ respectively reflect the charge excitation and spin excitation, and can be directly measured experimentally. Numerically, the dynamic excitation spectra can be computed using the stochastic maximum entropy algorithm [38, 54–56] based on $G(\mathbf{k}, \tau) = (1/\pi) \int d\omega A(\mathbf{k}, \omega) e^{-\tau\omega}$ and $S(\mathbf{k}, \tau) = (1/\pi) \int d\omega S(\mathbf{k}, \omega) e^{-\tau\omega}$. The numerical results of the single-particle spectral functions $A(\mathbf{k}, \omega)$ for $L = 12$ system are shown in the upper panel of Fig. 6 using different

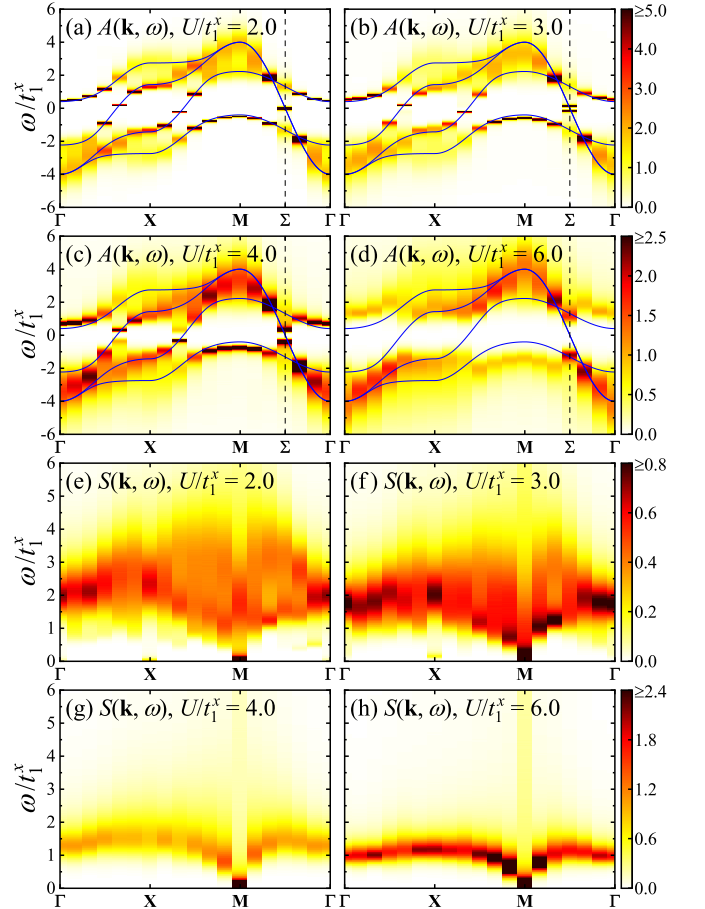


FIG. 6. (a-d) Single-particle spectra and (e-h) dynamic spin structure factors along high-symmetry path at different U/t_1^x . The solid lines in (a-d) are the noninteracting band structures.

U . When U is small like $U/t_1^x = 2.0$, there exist well-defined quasiparticles near the Fermi level, while the high energy part becomes incoherence. And the band dispersions still can be described well by the ones in the noninteracting limit. Moreover, a very small single-particle gap $\Delta_{\text{sp}}/t_1^x \approx 0.044$ is observed at Σ point, which is in good agreement with the value $\Delta_{\text{sp}}/t_1^x \approx 0.048$ extracted directly from $G(\mathbf{k}, \tau)$ [see Figs. 3(a) and 3(b)]. This single-particle gap will remain finite in the thermodynamic limit according to Fig. 3(b). As U increases, the single-particle gap also increases, and quasiparticles gradually disappear. Most interestingly, the lower Hubbard band near the Fermi level around the Γ and M which are entirely contributed from the $d_{3z^2-r^2}$ orbital gradually further move away from the Fermi level. And the deviation from the noninteracting band follows the same behavior as the gap opening in the Σ point. It is actually a Mottness behavior by shifting lower Hubbard band as U increases. The flatness of γ band is due to the strong localization of $d_{3z^2-r^2}$ orbitals.

The dynamic spin structure factors $(1/4)\sum_{\alpha} S^{\alpha}(\mathbf{k}, \omega)$ are shown in the lower panel of Fig. 6. In WI region, the spin gaps are very small [$O(10^{-2})t_1^x$] at Γ , X and M points, thus the expected gap is hard to visualize in the contour plot in Figs. 6(e) and 6(f). And the low-energy spectral weights at Γ and X are very weak compared to the M point. At higher energy, there is a broad continuum in the wide region of $\mathbf{k}-\omega$ plane with weak intensity due to “itinerant” weakly correlated electrons. As we increase interaction strength, the development of divergent spectral weight around $\omega/t_1^x = 0$ at M indicates the development of AFM order, while the low energy spectral weights around X and Γ eventually disappear and the dominant spectra become well-defined magnons.

Conclusion and discussion.—Using the large-scale DQMC simulations, we obtain the ground-state phase diagram, critical behavior and dynamical excitations of the simplified bilayer two-orbital Hubbard model at half filling. Between $U = 0$ metallic phase and $U > 4.15(10)$ antiferromagnetic Mott insulator, there is an intermediate weakly insulating phase without breaking any symmetries. This phase has weak charge and spin gaps and may be a bond nematic phase in the $d_{x^2-y^2}$ orbital and a interlayer dimer phase in the $d_{3z^2-r^2}$ orbital. The quantum phase transition between WI and AFMI belongs to 3D O(3) heisenberg universality class.

Even though this simplified model may deviate from the $\text{La}_3\text{Ni}_2\text{O}_7$ under ambient pressure, but they do share the similar Fermi surface and may have some common strong correlation features. For example, angle-resolved photoemission spectroscopy (ARPES) experiment has observed the flat $d_{3z^2-r^2}$ bonding band below the Fermi level exhibiting the strongest electron correlation, which is quite similar behavior seen in our single-particle spectral function. Furthermore, tuning the electron doping may drive the $\text{La}_3\text{Ni}_2\text{O}_7$ material into half-filling case [14]

where our results have already given some good predictions. In addition, it is noteworthy that some recent experimental measurements have revealed spin density wave instability with wave vector $(\pi/2, \pi/2)$ that may exist in $\text{La}_3\text{Ni}_2\text{O}_7$ under ambient pressure and low temperatures, which differs from the magnetic ordering in our work. This inconsistency can be attributed to the difference in electron filling of $d_{x^2-y^2}$ orbitals and . It is an interesting topic to reconsidering some neglected hopping terms and on-site potentials in the DQMC calculations. Then can we control the sign problem in DQMC to get useful information and to give a better understanding the fuzzy density wave in $\text{La}_3\text{Ni}_2\text{O}_7$ under ambient pressure? That is deserted for future study.

Acknowledgments.—We would like to thank Yi-Zhuang You, Wei Zhu, Wéi Wú and Zhihui Luo for helpful discussions. This project is supported by NKRDPC-2022YFA1402802, NSFC-11804401, NSFC-92165204, Leading Talent Program of Guangdong Special Projects (201626003), Guangdong Basic and Applied Basic Research Foundation (No.2023B1515120013), and Youth S&T Talent Support Programme of Guangdong Provincial Association for Science and Technology (GDSTA) (No. SKXRC202404). The calculations reported were performed on resources provided by the Guangdong Provincial Key Laboratory of Magnetoelectric Physics and Devices, No. 2022B1212010008.

* yaodaox@mail.sysu.edu.cn

† wuhanq3@mail.sysu.edu.cn

- [1] H. Sun, M. Huo, X. Hu, J. Li, Z. Liu, Y. Han, L. Tang, Z. Mao, P. Yang, B. Wang, J. Cheng, D.-X. Yao, G.-M. Zhang, and M. Wang, Signatures of superconductivity near 80 K in a nickelate under high pressure, *Nature* **621**, 493 (2023).
- [2] Z. Luo, X. Hu, M. Wang, W. Wú, and D.-X. Yao, Bilayer two-orbital model of $\text{La}_3\text{Ni}_2\text{O}_7$ under pressure, *Phys. Rev. Lett.* **131**, 126001 (2023).
- [3] J. Hou, P.-T. Yang, Z.-Y. Liu, J.-Y. Li, P.-F. Shan, L. Ma, G. Wang, N.-N. Wang, H.-Z. Guo, J.-P. Sun, Y. Uwatoko, M. Wang, G.-M. Zhang, B.-S. Wang, and J.-G. Cheng, Emergence of high-temperature superconducting phase in pressurized $\text{La}_3\text{Ni}_2\text{O}_7$ crystals, *Chin. Phys. Lett.* **40**, 117302 (2023).
- [4] Y. Zhang, D. Su, Y. Huang, Z. Shan, H. Sun, M. Huo, K. Ye, J. Zhang, Z. Yang, Y. Xu, Y. Su, R. Li, M. Smidman, M. Wang, L. Jiao, and H. Yuan, High-temperature superconductivity with zero resistance and strange-metal behaviour in $\text{La}_3\text{Ni}_2\text{O}_{7-\delta}$, *Nat. Phys.* (2024).
- [5] Y. Zhou, J. Guo, S. Cai, H. Sun, P. Wang, J. Zhao, J. Han, X. Chen, Y. Chen, Q. Wu, Y. Ding, T. Xiang, H. kwang Mao, and L. Sun, Investigations of key issues on the reproducibility of high- T_c superconductivity emerging from compressed $\text{La}_3\text{Ni}_2\text{O}_7$ (2024), [arXiv:2311.12361](https://arxiv.org/abs/2311.12361) [cond-mat.supr-con].
- [6] J. Li, P. Ma, H. Zhang, X. Huang, C. Huang, M. Huo, D. Hu, Z. Dong, C. He, J. Liao, X. Chen, T. Xie, H. Sun,

- and M. Wang, Pressure-driven right-triangle shape superconductivity in bilayer nickelate $\text{La}_3\text{Ni}_2\text{O}_7$ (2024), [arXiv:2404.11369 \[cond-mat.supr-con\]](#).
- [7] M. Zhang, C. Pei, Q. Wang, Y. Zhao, C. Li, W. Cao, S. Zhu, J. Wu, and Y. Qi, Effects of pressure and doping on Ruddlesden-Popper phases $\text{La}_{n+1}\text{Ni}_n\text{O}_{3n+1}$, *J. Mater. Sci. Technol.* **185**, 147 (2024).
- [8] G. Wang, N. N. Wang, X. L. Shen, J. Hou, L. Ma, L. F. Shi, Z. A. Ren, Y. D. Gu, H. M. Ma, P. T. Yang, Z. Y. Liu, H. Z. Guo, J. P. Sun, G. M. Zhang, S. Calder, J.-Q. Yan, B. S. Wang, Y. Uwatoko, and J.-G. Cheng, Pressure-induced superconductivity in polycrystalline $\text{La}_3\text{Ni}_2\text{O}_{7-\delta}$, *Phys. Rev. X* **14**, 011040 (2024).
- [9] Y. Zhang, L.-F. Lin, A. Moreo, T. A. Maier, and E. Dagotto, Structural phase transition, s_{\pm} -wave pairing, and magnetic stripe order in bilayered superconductor $\text{La}_3\text{Ni}_2\text{O}_7$ under pressure, *Nat. Commun.* **15**, 2470 (2024).
- [10] Y. Gu, C. Le, Z. Yang, X. Wu, and J. Hu, Effective model and pairing tendency in bilayer Ni-based superconductor $\text{La}_3\text{Ni}_2\text{O}_7$ (2023), [arXiv:2306.07275 \[cond-mat.supr-con\]](#).
- [11] Y.-B. Liu, J.-W. Mei, F. Ye, W.-Q. Chen, and F. Yang, s^{\pm} -Wave pairing and the destructive role of apical-oxygen deficiencies in $\text{La}_3\text{Ni}_2\text{O}_7$ under pressure, *Phys. Rev. Lett.* **131**, 236002 (2023).
- [12] Q.-G. Yang, D. Wang, and Q.-H. Wang, Possible s_{\pm} -wave superconductivity in $\text{La}_3\text{Ni}_2\text{O}_7$, *Phys. Rev. B* **108**, L140505 (2023).
- [13] H. Sakakibara, N. Kitamine, M. Ochi, and K. Kuroki, Possible high T_c superconductivity in $\text{La}_3\text{Ni}_2\text{O}_7$ under high pressure through manifestation of a nearly half-filled bilayer Hubbard model, *Phys. Rev. Lett.* **132**, 106002 (2024).
- [14] Z. Luo, B. Lv, M. Wang, W. Wú, and D.-X. Yao, High- T_c superconductivity in $\text{La}_3\text{Ni}_2\text{O}_7$ based on the bilayer two-orbital t-J model (2023), [arXiv:2308.16564 \[cond-mat.supr-con\]](#).
- [15] Y. Zhang, L.-F. Lin, A. Moreo, T. A. Maier, and E. Dagotto, Trends in electronic structures and s_{\pm} -wave pairing for the rare-earth series in bilayer nickelate superconductor $R_3\text{Ni}_2\text{O}_7$, *Phys. Rev. B* **108**, 165141 (2023).
- [16] Y.-H. Tian, Y. Chen, J.-M. Wang, R.-Q. He, and Z.-Y. Lu, Correlation effects and concomitant two-orbital s_{\pm} -wave superconductivity in $\text{La}_3\text{Ni}_2\text{O}_7$ under high pressure, *Phys. Rev. B* **109**, 165154 (2024).
- [17] Q. Qin and Y.-f. Yang, High- T_c superconductivity by mobilizing local spin singlets and possible route to higher T_c in pressurized $\text{La}_3\text{Ni}_2\text{O}_7$, *Phys. Rev. B* **108**, L140504 (2023).
- [18] J. Huang, Z. D. Wang, and T. Zhou, Impurity and vortex states in the bilayer high-temperature superconductor $\text{La}_3\text{Ni}_2\text{O}_7$, *Phys. Rev. B* **108**, 174501 (2023).
- [19] K. Jiang, Z. Wang, and F.-C. Zhang, High-temperature superconductivity in $\text{La}_3\text{Ni}_2\text{O}_7$, *Chin. Phys. Lett.* **41**, 017402 (2024).
- [20] H. Liu, C. Xia, S. Zhou, and H. Chen, Role of crystal-field-splitting and long-range-hoppings on superconducting pairing symmetry of $\text{La}_3\text{Ni}_2\text{O}_7$ (2023), [arXiv:2311.07316 \[cond-mat.supr-con\]](#).
- [21] Z. Fan, J.-F. Zhang, B. Zhan, D. Lv, X.-Y. Jiang, B. Normand, and T. Xiang, Superconductivity in nickelate and cuprate superconductors with strong bilayer coupling, *Phys. Rev. B* **110**, 024514 (2024).
- [22] R. Jiang, J. Hou, Z. Fan, Z.-J. Lang, and W. Ku, Pressure driven fractionalization of ionic spins results in cuprate-like high- T_c superconductivity in $\text{La}_3\text{Ni}_2\text{O}_7$, *Phys. Rev. Lett.* **132**, 126503 (2024).
- [23] C. Lu, Z. Pan, F. Yang, and C. Wu, Interlayer-coupling-driven high-temperature superconductivity in $\text{La}_3\text{Ni}_2\text{O}_7$ under pressure, *Phys. Rev. Lett.* **132**, 146002 (2024).
- [24] X.-Z. Qu, D.-W. Qu, J. Chen, C. Wu, F. Yang, W. Li, and G. Su, Bilayer $t-J-J_{\perp}$ model and magnetically mediated pairing in the pressurized nickelate $\text{La}_3\text{Ni}_2\text{O}_7$, *Phys. Rev. Lett.* **132**, 036502 (2024).
- [25] M. Wang, H.-H. Wen, T. Wu, D.-X. Yao, and T. Xiang, Normal and superconducting properties of $\text{La}_3\text{Ni}_2\text{O}_7$, *Chin. Phys. Lett.* **41**, 077402 (2024).
- [26] D.-X. Yao, Theoretical study of $\text{La}_3\text{Ni}_2\text{O}_7$ and $\text{La}_4\text{Ni}_3\text{O}_{10}$, *Science & Technology Review*, 1 (2024).
- [27] Y.-Y. Zheng and W. Wú, Superconductivity in the bilayer two-orbital Hubbard model (2023), [arXiv:2312.03605 \[cond-mat.str-el\]](#).
- [28] W. Wú, Z. Luo, D.-X. Yao, and M. Wang, Superexchange and charge transfer in the nickelate superconductor $\text{La}_3\text{Ni}_2\text{O}_7$ under pressure, *Sci. China Phys. Mech. Astron.* **67**, 117402 (2024).
- [29] V. Christiansson, F. Petocchi, and P. Werner, Correlated electronic structure of $\text{La}_3\text{Ni}_2\text{O}_7$ under pressure, *Phys. Rev. Lett.* **131**, 206501 (2023).
- [30] Y. Shen, M. Qin, and G.-M. Zhang, Effective bilayer model Hamiltonian and density-matrix renormalization group study for the high- T_c superconductivity in $\text{La}_3\text{Ni}_2\text{O}_7$ under high pressure, *Chin. Phys. Lett.* **40**, 127401 (2023).
- [31] F. Lechermann, J. Gondolf, S. Bötzel, and I. M. Eremin, Electronic correlations and superconducting instability in $\text{La}_3\text{Ni}_2\text{O}_7$ under high pressure, *Phys. Rev. B* **108**, L201121 (2023).
- [32] Y.-f. Yang, G.-M. Zhang, and F.-C. Zhang, Interlayer valence bonds and two-component theory for high- T_c superconductivity of $\text{La}_3\text{Ni}_2\text{O}_7$ under pressure, *Phys. Rev. B* **108**, L201108 (2023).
- [33] Y. Chen, Y.-H. Tian, J.-M. Wang, R.-Q. He, and Z.-Y. Lu, Non-Fermi liquid and antiferromagnetic correlations with hole doping in the bilayer two-orbital Hubbard model of $\text{La}_3\text{Ni}_2\text{O}_7$ at zero temperature (2024), [arXiv:2407.13737 \[cond-mat.supr-con\]](#).
- [34] J. Yang, H. Sun, X. Hu, Y. Xie, T. Miao, H. Luo, H. Chen, B. Liang, W. Zhu, G. Qu, C.-Q. Chen, M. Huo, Y. Huang, S. Zhang, F. Zhang, F. Yang, Z. Wang, Q. Peng, H. Mao, G. Liu, Z. Xu, T. Qian, D.-X. Yao, M. Wang, L. Zhao, and X. J. Zhou, Orbital-dependent electron correlation in double-layer nickelate $\text{La}_3\text{Ni}_2\text{O}_7$, *Nat. Commun.* **15**, 4373 (2024).
- [35] Y. Wang, K. Jiang, Z. Wang, F.-C. Zhang, and J. Hu, The electronic and magnetic structures of bilayer $\text{La}_3\text{Ni}_2\text{O}_7$ at ambient pressure (2024), [arXiv:2401.15097 \[cond-mat.supr-con\]](#).
- [36] J. E. Hirsch, Two-dimensional Hubbard model: Numerical simulation study, *Phys. Rev. B* **31**, 4403 (1985).
- [37] F. F. Assaad and H. G. Evertz, World-line and determinantal quantum Monte Carlo methods for spins, phonons and electrons, in *Computational Many-Particle Physics*, edited by H. Fehske, R. Schneider, and A. Weiße (Springer Berlin Heidelberg, Berlin, Heidelberg, 2008) pp. 277–356.
- [38] F. F. Assaad, M. Bercx, F. Goth, A. Götz, J. S. Hofmann, E. Huffman, Z. Liu, F. P. Toldin, J. S. E. Portela, and

- J. Schwab, The ALF (Algorithms for Lattice Fermions) project release 2.0. Documentation for the auxiliary-field quantum Monte Carlo code, *SciPost Phys. Codebases*, **1** (2022).
- [39] Y. Otsuka, S. Yunoki, and S. Sorella, Universal quantum criticality in the metal-insulator transition of two-dimensional interacting Dirac electrons, *Phys. Rev. X* **6**, 011029 (2016).
- [40] S. S. Kancharla and S. Okamoto, Band insulator to Mott insulator transition in a bilayer Hubbard model, *Phys. Rev. B* **75**, 193103 (2007).
- [41] D. Tahara and M. Imada, Variational Monte Carlo study of electron differentiation around mott transition, *J. Phys. Soc. Jpn.* **77**, 093703 (2008).
- [42] M. Sentef, J. Kuneš, P. Werner, and A. P. Kampf, Correlations in a band insulator, *Phys. Rev. B* **80**, 155116 (2009).
- [43] A. Euverte, S. Chiesa, R. T. Scalettar, and G. G. Batrouni, Magnetic transition in a correlated band insulator, *Phys. Rev. B* **87**, 125141 (2013).
- [44] J. Wang, L. Zhang, R. Ma, Q. Chen, Y. Liang, and T. Ma, Intermediate phase in interacting Dirac fermions with staggered potential, *Phys. Rev. B* **101**, 245161 (2020).
- [45] V. Ayyar and S. Chandrasekharan, Massive fermions without fermion bilinear condensates, *Phys. Rev. D* **91**, 065035 (2015).
- [46] Y.-Y. He, H.-Q. Wu, Y.-Z. You, C. Xu, Z. Y. Meng, and Z.-Y. Lu, Quantum critical point of dirac fermion mass generation without spontaneous symmetry breaking, *Phys. Rev. B* **94**, 241111 (2016).
- [47] J. Wang and Y.-Z. You, Symmetric mass generation, *Symmetry* **14**, 1475 (2022).
- [48] D.-C. Lu, M. Li, Z.-Y. Zeng, W. Hou, J. Wang, F. Yang, and Y.-Z. You, Superconductivity from Doping Symmetric Mass Generation Insulators: Application to $\text{La}_3\text{Ni}_2\text{O}_7$ under Pressure (2023), [arXiv:2308.11195 \[cond-mat.supr-con\]](https://arxiv.org/abs/2308.11195).
- [49] W.-X. Chang, S. Guo, Y.-Z. You, and Z.-X. Li, Fermi surface symmetric mass generation: a quantum Monte-Carlo study (2023), [arXiv:2311.09970 \[cond-mat.str-el\]](https://arxiv.org/abs/2311.09970).
- [50] K. Harada, Bayesian inference in the scaling analysis of critical phenomena, *Phys. Rev. E* **84**, 056704 (2011).
- [51] K. Harada, Kernel method for corrections to scaling, *Phys. Rev. E* **92**, 012106 (2015).
- [52] M. Campostrini, M. Hasenbusch, A. Pelissetto, P. Rossi, and E. Vicari, Critical exponents and equation of state of the three-dimensional Heisenberg universality class, *Phys. Rev. B* **65**, 144520 (2002).
- [53] X. Jia, D.-X. Yao, and H.-Q. Wu, Phase diagram and critical behavior of the Hubbard model on the square-hexagon-octagon lattice, *Phys. Rev. B* **109**, 155122 (2024).
- [54] A. W. Sandvik, Stochastic method for analytic continuation of quantum Monte Carlo data, *Phys. Rev. B* **57**, 10287 (1998).
- [55] K. S. D. Beach, Identifying the maximum entropy method as a special limit of stochastic analytic continuation (2004), [arXiv:cond-mat/0403055 \[cond-mat.str-el\]](https://arxiv.org/abs/cond-mat/0403055).
- [56] H. Shao and A. W. Sandvik, Progress on stochastic analytic continuation of quantum Monte Carlo data, *Phys. Rep.* **1003**, 1 (2023).

Supplemental Material: Exploring the Phase Diagram and Correlation Effect in a Simplified Bilayer Two-Orbital Hubbard Model at Half Filling

I. FINITE-SIZE CLUSTERS USED IN THE SIMULATIONS

In the weakly interacting region, the Fermi surface is a key ingredient to determine the physical properties of the system. The clusters with small sizes may exhibit behaviors significantly different from large-size clusters due to their finite-size wavevectors are away from the Fermi surface in the Brillouin zone. In Fig. S1, we representatively show some finite-size wave vectors of some system sizes. The $M = (\pi, \pi)$ point is the magnetic Bragg peak position for large U . We consistently select clusters (under PBC) that encompass the M point within the Brillouin zone. The clusters used in the extrapolations of the AFM structure factor are $L \geq 10$ and $L' \geq 6$, whose momentum points are sufficiently dense and finite-size effect are not severe. Linear fittings are able to provide reliable extrapolations. In addition to the M point, to probe the single-particle energy gap at the Fermi surface, we also require that the finite-sized clusters we select include the $\Sigma = (\pi/2, \pi/2)$ point. In the main text, we use the single-particle gap at the Σ point to determine the weakly insulating phase. We use six finite-size clusters that contains two wavevectors, namely $L = 4, 8, 12$ and $L' = 4, 6, 8$, to do the extrapolations of gaps. However, strong finite-size effect still exist in the extrapolations of single-particle gap and spin gap. So we impose constrain in the extrapolations using second-order polynomial functions, ensuring that the fitting curves can be monotonically extrapolated to the $N_c \rightarrow \infty$ limit.

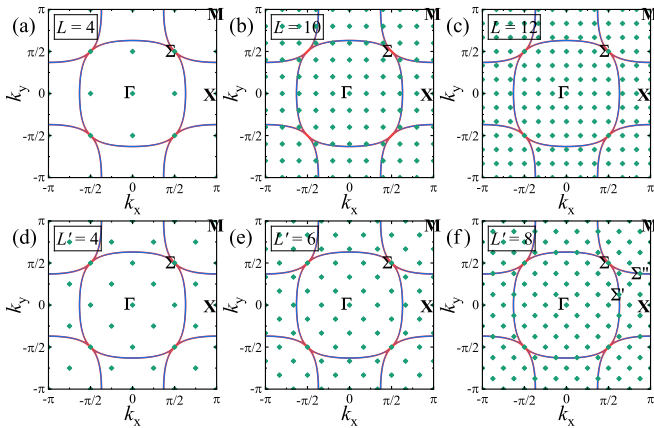


FIG. S1. The wavevector points of different finite-size clusters and the Fermi surfaces.

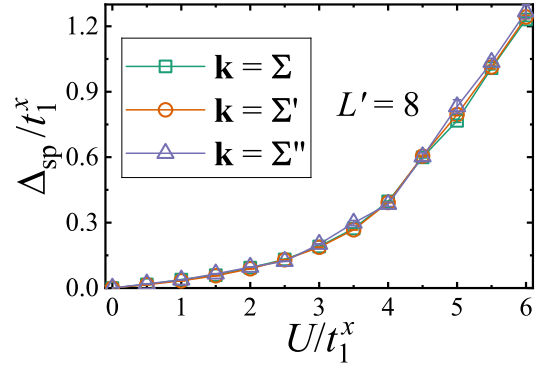


FIG. S2. The single-particle gaps at the Σ , Σ' , and Σ'' points as functions of U/t_1^x . The linear system size we used here is $L' = 8$ which contains these three wavevectors on the Fermi surface, as is shown in Fig. S1 (f).

II. SINGLE-PARTICLE GAPS OPEN SIMULTANEOUSLY ON THE FERMION SURFACE

As shown in Fig. S1(f), in the special linear system size $L' = 8$, the Σ' and Σ'' points are located on different Fermi pockets, while the Σ is at the contact point of two Fermi pockets. The single-particle gaps at these three points as functions of U are shown in Fig. S2. All of these gaps increase monotonically with U , and their values are nearly equal to each other. It is reasonable to conclude that the entire Fermi surface opens the single-particle gap simultaneously at $U > 0$. Therefore, the spectral gap at the Σ point can faithfully represent the single-particle gap of the system.

III. ABSENCE OF CONVENTIONAL ORDERS IN THE WEAKLY INSULATING PHASE

Our numerical results indicate that the system is a non-magnetic insulating phase in the weakly interacting ($0 < U < U_c$) region, even with a small finite spin gap. It is dominated by the interlayer singlet prod-

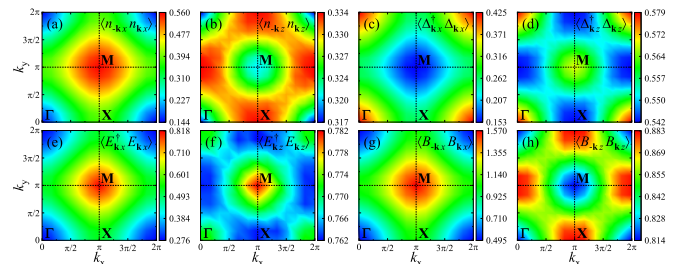


FIG. S3. Contour plots of static structure factors for (a-b) charge density wave, (c-d) pairing density wave, (e-f) excitation, and (g-h) bond order wave, with $L = 12$ and $U/t_1^x = 3.0$. The subscripts x and z denote the $d_{x^2-y^2}$ and $d_{3z^2-r^2}$ orbitals, respectively.

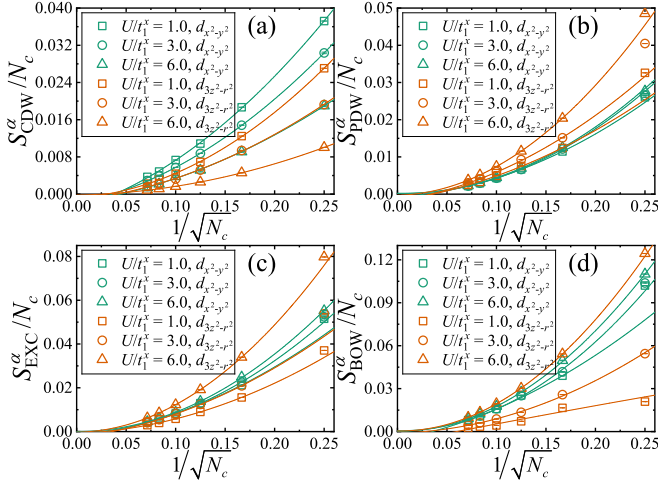


FIG. S4. Extrapolations of different structure factors. (a) charge density wave; (b) pairing density wave; (c) exciton; (d) bond order wave.

uct state of $d_{3z^2-r^2}$ orbitals. We have examined the local spin correlations $\langle \mathbf{S}_{i\alpha} \cdot \mathbf{S}_{j\lambda} \rangle$ and local hopping terms $\sum_{\sigma} \langle (c_{i\alpha\sigma}^{\dagger} c_{j\lambda\sigma} + H.c.) \rangle$ of finite-size system under open boundary condition. And we didn't see the inplane valence bond solid like patterns.

To exclude some other conventional orders like charge density wave (CDW), pairing density wave (PDW), exciton (EXC), and bond order wave (BOW), we have also calculate their corresponding static structure factors, which are defined as

$$\begin{aligned} S_{\text{CDW}}^{\alpha}(\mathbf{k}) &= \langle n_{-\mathbf{k}\alpha} n_{\mathbf{k}\alpha} \rangle \\ &= \frac{1}{N_c} \sum_{i,j} e^{-i\mathbf{k} \cdot (\mathbf{R}_j - \mathbf{R}_i)} \langle n_{i\alpha} n_{j\alpha} \rangle, \end{aligned}$$

$$\begin{aligned} S_{\text{PDW}}^{\alpha}(\mathbf{k}) &= \langle \Delta_{\mathbf{k}\alpha}^{\dagger} \Delta_{\mathbf{k}\alpha} \rangle \\ &= \frac{1}{N_c} \sum_{i,j} e^{-i\mathbf{k} \cdot (\mathbf{R}_j - \mathbf{R}_i)} \langle \Delta_{i\alpha}^{\dagger} \Delta_{j\alpha} \rangle, \end{aligned}$$

$$\begin{aligned} S_{\text{EXC}}^{\alpha}(\mathbf{k}) &= \langle E_{\mathbf{k}\alpha}^{\dagger} E_{\mathbf{k}\alpha} \rangle \\ &= \frac{1}{N_c} \sum_{i,j} e^{-i\mathbf{k} \cdot (\mathbf{R}_j - \mathbf{R}_i)} \langle E_{i\alpha}^{\dagger} E_{j\alpha} \rangle, \end{aligned}$$

$$\begin{aligned} S_{\text{BOW}}^{\alpha}(\mathbf{k}) &= \langle B_{-\mathbf{k}\alpha} B_{\mathbf{k}\alpha} \rangle \\ &= \frac{1}{N_c} \sum_{i,j} e^{-i\mathbf{k} \cdot (\mathbf{R}_j - \mathbf{R}_i)} \langle B_{i\alpha} B_{j\alpha} \rangle, \end{aligned}$$

where $n_{i\alpha} = \sum_{\sigma} n_{i\alpha\sigma}$. Their peak positions can be found in Fig. S3, we can use these peaks to do the extrapolations. However, no CDW, PDW, EXC and BOW orders were found, as can be seen in Fig. S4.

IV. SUPPRESSING MAGNETIC CORRELATION BY INTERLAYER HOPPING t_{\perp}^z AND HYBRIDIZATION HOPPING t_3^{xz}

To further study the effects of interlayer hopping t_{\perp}^z and the hybridization hopping t_3^{xz} . We have calculate the static spin structure factors at M point as functions of t_{\perp}^z/t_1^x while keeping $t_3^{xz}/t_1^x = 0.495$ fixed, which are shown in Fig. S5 (a). We can see that increasing t_{\perp}^z would strongly suppress the magnetic correlation in $d_{3z^2-r^2}$ orbital. For varying t_3^{xz} while keeping $t_{\perp}^z = 1.315$ fixed, the spin correlation in $d_{x^2-y^2}$ orbital is suppressed. For the $d_{3z^2-r^2}$ orbital, due to strong local interlayer correlation induced by U and large t_{\perp}^z , the spin structure factor is very small and nearly unchange with t_3^{xz} .

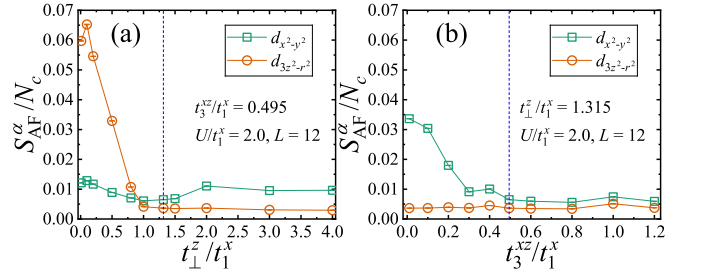


FIG. S5. Static spin structure factors at M point as functions of (a) t_{\perp}^z/t_1^x and (b) t_3^{xz}/t_1^x , respectively. When we alter the value of one variable, either t_{\perp}^z or t_3^{xz} , we maintain the value of the other constant. And these results are obtained on a $L = 12$ cluster.